UNIVERSITY OF ZARAGOZA

Faculty of Science

Final Master's Project

Slow Magnetic Relaxation of Dysprosium(III) Molecular Magnets

Author:

Yonatan Ashlea Alava

Supervisor:

Fernando Bartolomé Usieto

June 2017

Universidad Zaragoza

icma Instituto de Ciencia de Materiales de Aragón

Instituto Universitario de Investigación en Nanociencia de Aragón

Universidad Zaragoza

TABLE OF CONTENTS

Chapter 1. Introduction and objectives

A molecular magnet is a nano-sized magnet composed of a molecule containing one magnetic ion (Single-Ion Molecule Magnet SIMMs) or more (polynuclear Single-Molecule Magnet SMMs) which provide the molecule with magnetic properties.

One may consider that the field of molecular magnetism was born in 1993 with the discovery by Sessoli et al. [1] of a twelve-ion manganese cluster known as Mn_{12}, which possessed magnetic properties akin to that of superparamagnetic materials. This molecule, synthesised years earlier by Lis, T. [2], showed a high magnetic anisotropy; when a magnetic field was applied parallel to the crystallographic symmetry axis, the magnetisation was much higher than when applied perpendicular to the crystallographic symmetry axis. This anisotropy was associated to an anisotropy barrier which prevented the magnetic moment of the molecule from transitioning to the ground state (relaxation) when the magnetic field was switched off. The magnetic moment eventually relaxed to the ground state after 2 months when the system was at $T = 2$ K. This period of time is known as relaxation time, τ. Interestingly, it was observed to vary with the temperature following Arrhenius' law: $\ln(\tau) \propto 1/T$. The authors attributed this slow relaxation time to the "freezing" of the magnetisation below 3 K on the timescale of the experiment. This temperature is known as the blocking temperature, T_B. The compound also exhibited an open hysteresis loop below this temperature, which implied a stable magnetisation at a magnetic field of 1 T, and a reversal of this magnetisation only at a magnetic field of 1 T in the opposite direction. As a consequence, there were two stable magnetisation states below 3 K, a phenomenon known as magnetic bistability. In view of their results, the authors suggested that these types of molecules could be useful for information storage since the magnetisation could be preserved over long periods of time. Furthermore, the small size of the molecules seemed ideal to achieve dense magnetic memory devices.

These results seeded the field of molecular magnetism and a race to obtain better properties began; higher anisotropy barriers that would lead to longer relaxation times, and more accessible (higher) blocking temperatures[1] below which the magnetisation freezes. Molecular magnets containing transition metals, such as the Mn_{12} previously described, were sidelined by the use of a different type

[1] T_B is an ill-defined parameter since it depends on the sweeping rate of the magnetic field. There should be an aim at reaching a consensus for the magnitude of the sweeping rate.

of magnetic ions which would provide even higher anisotropy barriers and blocking temperatures due to their intrinsically large orbital momentum. These magnetic ions are lanthanides/rare earth ions [3]. Within the lanthanide-based realm of molecules, the most important are single-ion and polynuclear molecules. Currently, the record-holding magnetic molecule in terms of highest anisotropy barrier is a single-ion molecule ($[\mathrm{Dy(bbpen)Br}]$) discovered by Liu et al. [4] with an anisotropy barrier of $\Delta/k_B = 1025$ K. Another compound[2] ($[\mathrm{DyL_2(H_2O)Br}]$), characterised by Gupta et al. [5] exhibited the highest blocking temperature measured (as of 2017) of $T_B = 30$ K at a sweeping rate of $200\ \mathrm{Oe/s}$. In terms of polynuclear magnetic molecules, the anisotropy barrier height record is set at $\Delta/k_B = 842$ K [6] for $[\mathrm{Dy_4K_2O}]$ and the highest blocking temperature at $T_B = 16$ K at a sweeping rate of $1400\ \mathrm{Oe/s}$ [7] for $[\mathrm{Dy_4(bzhdep-2H)_4}]$. Despite these astonishing magnetic properties, there is a big issue in the field: a vast number of molecules present very high anisotropy barriers but very low blocking temperatures and therefore non-accessible magnetic bistability, which renders them of little use in terms of applications.

Several applications for molecular magnets have been proposed over the years, encouraging scientists of different fields: inorganic chemistry, physical chemistry, condensed matter physics among others, to carry out thorough research on this quest. Recent advances have achieved transferring single-molecule magnets onto surfaces without the loss of magnetic properties [8]. This opens up the possibility of applications in spintronics [9], in which the spin of the molecule is used to carry information, as proposed by Candini et al. [10]. Moreover, Leuenberger et al. [11] proposed the use of molecular magnets for quantum computing as quantum bits due to their large magnetic moments.

There are two objectives in this project, academic and scientific. The former involves the realisation of the project for the completion of a one-year Master's Degree in "Nanostructured Materials for Nanotechnology Applications" to enable students to experience research in an academic environment, and form both individual and team-work skills. The second is specific to this project and entails the physical characterisation of two newly-synthesised polynuclear Dysprosium(III) magnetic molecules, and assess whether they present interesting magnetic properties for the aforementioned potential applications of molecular magnets.

[2] For the full name of the complexes, see the corresponding cited references.

Chapter 2. Background theory

2.1 Origin of the anisotropy in molecular magnets

Magnetic anisotropy occurs when a system has preferred orientations for its magnetic moment. The origin of the magnetic anisotropy in molecular magnets is described next.

The magnetic anisotropy in a molecular magnet is caused by the intrinsic spin-orbit coupling within the magnetic ion and its interaction with an electric crystal field, created by the environment of the magnetic ion.

Solving the Hamiltonian of the system including these two latter effects will reveal the magnetic anisotropy of the system. The Hamiltonian can be written as:

$$H = H_0 + H_{e-e} + H_{SO} + H_{CF} \quad (1)$$

where H_0 is the hydrogen-like Hamiltonian, H_{e-e} accounts for the correlation between electrons, H_{SO} is the spin-orbit interaction term and H_{CF} describes the interaction of the ion with the electric fields caused by the ligands which form the environment of the ion.

The electron correlation term modifies the hydrogen-like energy levels following Hund's first and second rules [12]. In the case of Dy(III), the $4f^9$ electronic configuration is modified by Hund's rules. In effect, Hund's maximum total spin multiplicity (1st rule) dictates a total spin: $S = \sum s_z = 5/2$ and maximum total orbital momentum (2nd rule): $L = \sum l_z = 5$. This yields $^{2S+1}L \equiv {}^6H$ as the ground state level (Figure 1).

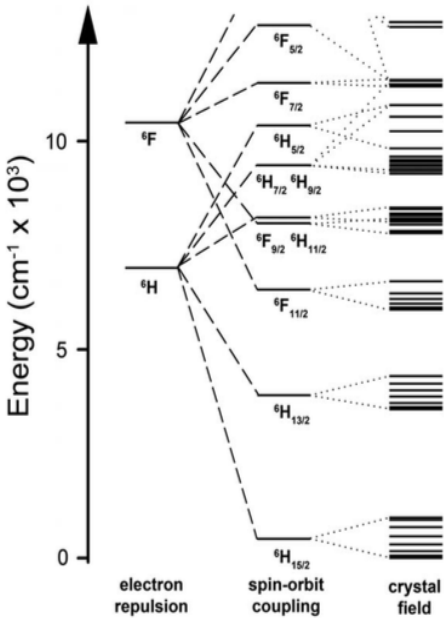

Figure 1. Energy levels reconstruction for the complex $Dy[(Me_3Si)_2N]_3$ solving the Hamiltonian in equation (1) for this particular complex (Adapted from [3]).

The spin-orbit coupling term modifies the levels even further distinguishing total angular momentum states J. Hund's third rule dictates the coupling $\mathbf{J = L + S}$ known as Russel-Saunders coupling[3]: $J = 15/2$. This yields a ground state for the Dy(III) ion of $^{2S+1}L_J \equiv {}^6H_{15/2}$ (Figure 1).

[3] The Russel-Saunders coupling was proposed for light atoms up to Sn (Z=50). The j-j coupling usually works best for heavier atoms. However, it was proven that the Russel-Saunders coupling works well for rare earths [36].

The crystal field lifts the degeneracy of the $J = 15/2$ ground state into its z projections $J_z = -15/2, -13/2, \ldots, 13/2, 15/2$. The reason is the that Coulomb repulsion of the ligands affects differently each J_z because of how each J_z is oriented in space.

The ground state is split into 8 doublets following Kramers' Theorem, which splits the levels into doublets for ions with an odd number of electrons [13].

The doublets have the same energy. However, there is an energy barrier (anisotropy barrier) between them:

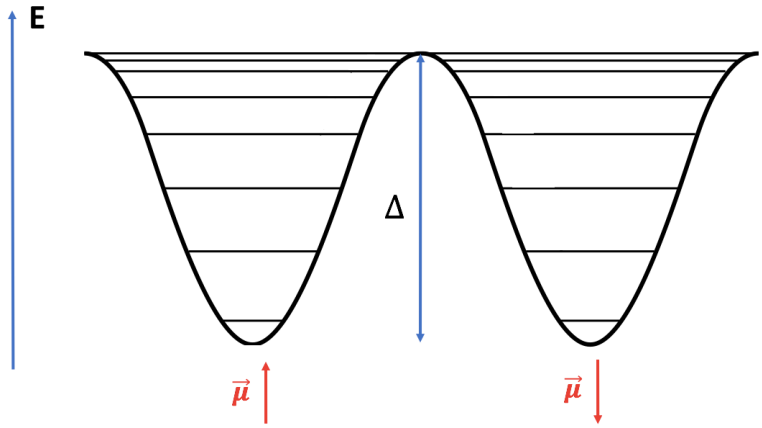

Figure 2. Qualitative depiction of the energy barrier, Δ, also known as anisotropy barrier. $\vec{\mu}$ is the magnetic moment pointing in the direction of the arrow for each state.

If the system is in the $J_z = -15/2$ state it must overcome the anisotropy barrier Δ, to arrive at the equally energetic state $J_z = +15/2$ state. The existence of an anisotropy barrier can be intuitively understood in a simplified manner for a single ion in its environment as follows (see Figure 3):

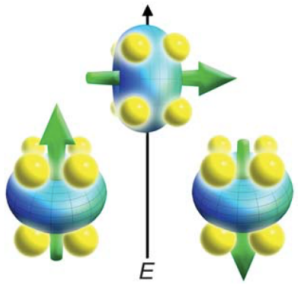

Figure 3. The blue spheroid represents the electron density in the 4f atomic shell. The yellow spheres represent charge centres of the ligands. Left and right: the state is energetically favourable because the electrostatic repulsion between the ligand charges and the 4f electron density is minimised due to the shape and location of the charged centres. Centre: the Coulomb repulsion is higher and therefore it is a more energetic state (adapted from [3]).

The magnetic moment on the left (Figure 3) must physically rotate through electrostatic repulsion (anisotropy barrier) to arrive at the equally energetic state on the right.

The preferred orientations for the magnetic moment discussed at the beginning of this section are precisely the magnetic moments in the doubly-degenerate ground state.

2.2 Paramagnetism in molecular magnets

The magnetic moment of an atom is proportional to its total angular momentum **J** [14]:

$$\boldsymbol{\mu} = \mu_B g \boldsymbol{J} \tag{2}$$

where $\boldsymbol{\mu}$ is the magnetic moment of the atom, μ_B is the Bohr magneton and g is the gyromagnetic factor (g-factor). In the case of lanthanide ions, which have S, L and J, the g-factor takes the following form under a weak applied field[4]:

$$g_J = \frac{3}{2} + \frac{S(S+1) - L(L+1)}{2J(J+1)} \tag{3}$$

where g_J is known as the Landé g-factor.

Magnetic moments of ions within molecules are the cause for the molecule's paramagnetic nature. In these paramagnetic molecules, the magnetic moments are oriented in random directions that change in time and space in the absence of an externally applied magnetic field. This is because the magnetic moments interact weakly with each other and can be considered independent at room temperature. The magnetic moments orient themselves along the direction of the applied field, producing a net magnetization of the system that increases with the magnitude of the externally applied magnetic field [14].

An increase in the applied magnetic field increases the magnetisation of the paramagnetic system because it induces the aligning with the field of partially aligned magnetic moments. On the contrary, an increase in temperature randomises the direction of the magnetic moments. A quantum mechanical treatment of the system using statistical mechanics leads to an expression for the magnetisation of a paramagnetic system [14]:

$$M = n g_J \mu_B J B_J(y) \tag{4}$$

where n is the number of magnetic atoms per unit volume, g_J the gyromagnetic factor, μ_B is the Bohr magneton, J is the total angular momentum quantum number of the paramagnetic atoms and $B_J(y)$ is known as the Brillouin function, which reads:

$$B_J(y) = \frac{2J+1}{2J}\coth\left(\frac{2J+1}{2J}y\right) - \frac{1}{2J}\coth\frac{y}{2J} \tag{5}$$

where $y = g_J \mu_B JB/k_B T$, k_B is Boltzmann's constant and T is temperature.

For systems in which $y \ll 1$, that is, for all systems except those at very low temperatures and/or extremely large magnetic fields, the Brillouin function can be simplified using the Maclaurin expansion of $\coth(y)$:

$$B_J = \frac{(J+1)y}{3J} + O(y^3) \tag{6}$$

This yields a magnetic susceptibility that follows the Curie Law (in SI units):

[4] "Field" refers to "magnetic field" throughout the document, for practical purposes.

$$\chi = \frac{M}{H} \approx \frac{\mu_0 M}{B} = \frac{n\mu_0 \mu_{\text{eff}}^2}{3k_B T} \tag{7}$$

where μ_0 is the magnetic permeability in vacuum, k_B is Boltzmann's constant, H is the magnetic field intensity and μ_{eff} is an effective magnetic moment of the paramagnetic atoms, which takes the form [14]:

$$\mu_{\text{eff}} = g_J \mu_B \sqrt{J(J+1)} \tag{8}$$

in the limit of vanishing magnetic fields[5].

2.3 Paramagnetic relaxation

When an external magnetic field is applied, the energy levels in Figure 1 are further split through the Zeeman splitting, which is modelled via the Zeeman Hamiltonian [14]. The anisotropy barrier is modified since the magnetic field lifts the degeneracy of the doublets:

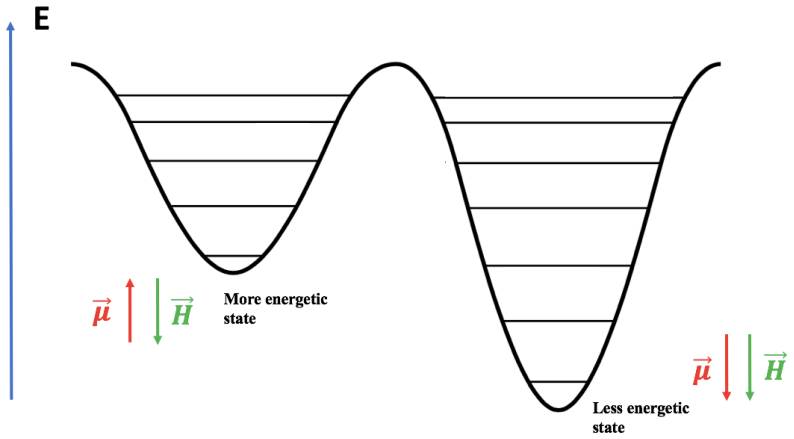

Figure 4. Degeneracy lift of the doublets when an external magnetic field $\vec{H}$, is applied. The states to the left are turned more energetic since the field and the magnetic moment in those states are antiparallel. The states to the right are less energetic because the field and the magnetic moments are parallel (adapted from [15]).

If the system initially has its magnetic moments parallel to the applied magnetic field, when the field is inverted in direction, the initial state becomes more energetic (magnetic moments antiparallel to the field) and the less energetic/equilibrium state has the magnetic moments parallel to the field. The system will attempt to transition to the latter lower-energy state. This is known as magnetic relaxation, and is characterised by how long it takes the system to relax, described by the relaxation time, τ.

The system of magnetic moments is commonly referred to as spin system, whereas its thermal environment is known as the lattice. The spin system and the lattice are in contact with a thermal bath (usually Helium bath). Waller [16] was the first to point out that there are two main relaxation mechanisms; via spin-spin interactions and spin-lattice interactions. The latter will be discussed in

[5] When the field is non-negligible and the magnetisation has saturated, the formula $\mu_{\text{eff}} = g_J \mu_B J$ is used.

this dissertation (see Ref [17]). Spin-lattice interactions are thermal exchanges between the paramagnetic system and the environment of the molecule. When a magnetic field is applied, the spin of the molecules aligns with the field. In this process, heat is released from the spin system to the lattice because it transitions from a higher to a lower energy state.

These heat exchanges are understood in quantum physics as phonon-exchange processes; electrons in the magnetic ions absorb/emit phonons in order to rearrange the populations of certain energy levels to acquire thermal equilibrium, and therefore an equilibrium magnetisation under the new conditions. The time variation of the magnetisation can be modelled phenomenologically in the following manner [17]:

$$\frac{\partial M}{\partial t} = \frac{M_0 - M}{\tau} \tag{9}$$

where M_0 is the equilibrium magnetisation, M the varying magnetisation, t, is time and τ is the relaxation time. This formula implies that the time variation of the magnetisation is inversely proportional to the relaxation time. If the relaxation is fast (low relaxation time), the rate at which the magnetisation changes is high, and vice versa.

There are three main types of thermal relaxation mechanisms; direct, Orbach and Raman. Direct processes involve the emission of a single phonon from the initial state $|2\rangle$ to the final state $|1\rangle$, with the correct energy $\hbar\omega = \Delta_{2\to1}$ to enable the spin transition. Two phonons are involved in a Raman relaxation process: a phonon is absorbed taking the system to a so-called "virtual state" $|\vartheta\rangle$, followed by the emission of a phonon $\hbar\omega_s$, relaxing the system to the ground state, $|1\rangle$. In an Orbach process, a phonon is absorbed and excites the system to a higher electronic level $|3\rangle$, to then emit a phonon of energy $\hbar\omega = \Delta_{3\to1}$, relaxing to the ground state [18]. Each process has a specific dependence on temperature and the magnetic field (see Appendix to Chapter 2 , page 31).

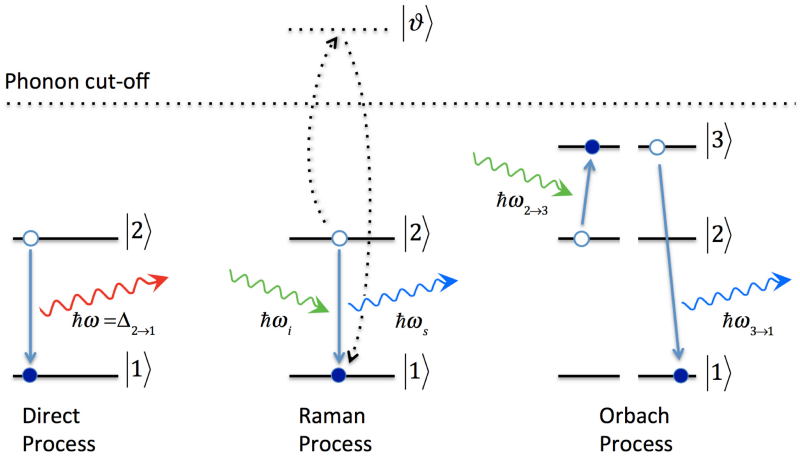

Figure 5. Direct, Raman and Orbach relaxation processes. $|2\rangle$, $|1\rangle$ are the initial and final states respectively. $|\vartheta\rangle$, is an intermediate state involved in the Raman relaxation process. $|3\rangle$ is the first higher electronic level above the initial state in the Orbach process. The red and blue wavy arrows represent emitted phonons whereas the green ones represent absorbed phonons. The phonon cut-off represents the highest energy phonon possible, which is limited by the minimum length between the atoms in the system.

Friedman et al. [19] first reported a different relaxation mechanism: magnetic quantum tunnelling (MQT), in Mn_{12} molecules. This relaxation pathway was observed to be much quicker than thermal relaxation mechanisms: $\tau_{tun} \sim 10^{-8} s$ whereas $\tau_{spin\text{-}lattice} \sim 10^{-2}\ s$ usually.

2.4 Magnetic bistability in molecular magnets

When the relaxation time of a molecular magnet is shorter than the timescale of the experiment, open magnetic hysteresis occurs. This is because the molecules have not been able to relax by the time the field is swept towards 0 and thus a non-zero magnetisation remains. This phenomenon is known as magnetic bistability due to the two stable magnetisation states at 0 field (see Figure 6).

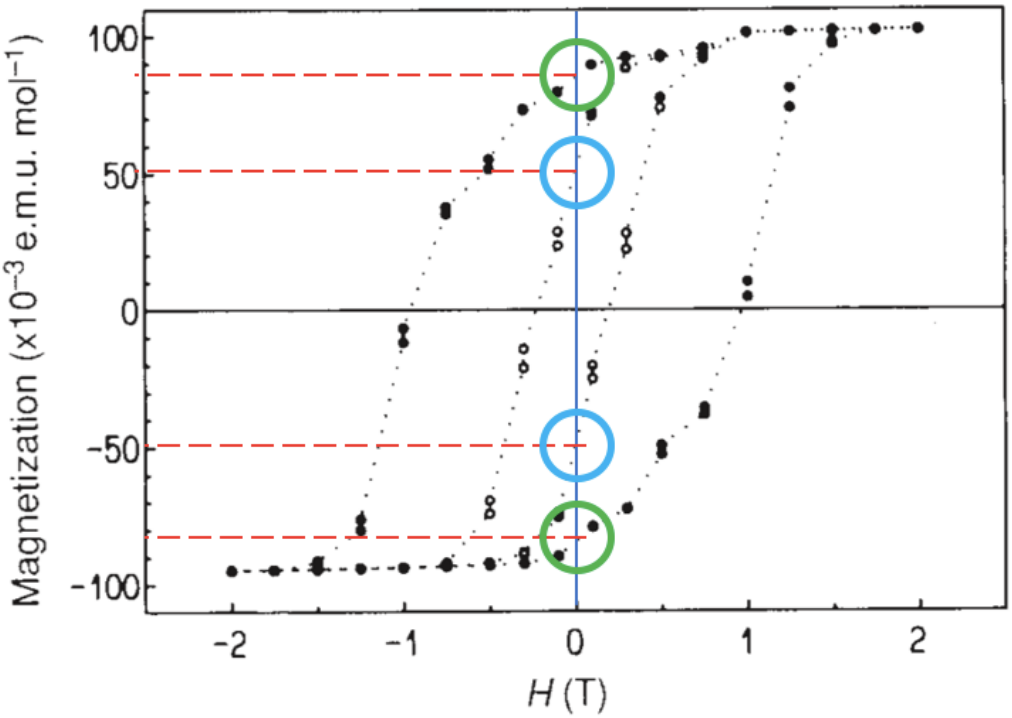

Figure 6. Open magnetic hysteresis. The hysteresis loop is more open for the 2,2 K measurements (filled symbols) and narrows for the 2,8 K measurements (empty symbols). The green circles indicate the bistable states at T = 2,2 K and the blue circles at T = 2,8 K. The relaxation time was measured to be 2 months, which is significantly longer than any experiment timescale. The sweeping rate applied was approximately 3,5 Oe/s Adapted from [1].

The hysteresis loop is more open at lower temperatures. Also, the coercive field increases meaning a higher magnetic field must be applied in the inverse direction to supress the magnetisation at lower temperatures.

2.5 Motivation for using Lanthanide ions

As mentioned previously, slow relaxation times are desirable for potential applications. Thus, researchers in the field have been aiming at acquiring molecules with high energy barriers (and hence

slow relaxation times) and open hysteresis loops at more accessible temperatures, i.e. higher blocking temperatures.

Lanthanide-based molecules have been shown to present higher anisotropy barriers than transition metal clusters [3], and the latter have thereafter been overshadowed by lanthanide-based molecules in the past years.

In fact, blocking temperatures and anisotropy barriers have increased from 3 to 30 K and $U_{eff} = 62$ K to 1025 K respectively[6]. Such molecules usually contain dysprosium (Dy), Terbium, (Tb) or Erbium (Er) ions. The reason lanthanides are of interest rests on the fact that they possess a large orbital angular momentum **L** due to having incomplete 4f shells, which leads to a high intrinsic anisotropy. Also, Rinehart et al. [3] proposed that the anisotropy barrier can be further increased by judiciously choosing the coordination environment of the magnetic ions.

Bartolomé et al. [20] gathered data of the highest blocking temperatures and anisotropy barriers achieved in molecular magnets as of May 2017:

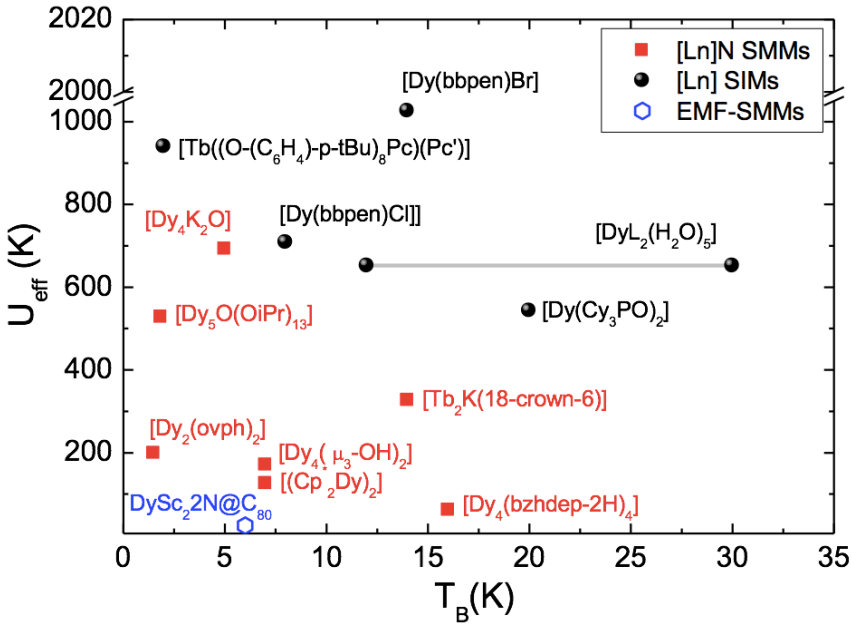

Figure 7. Highest anisotropy barriers U_{eff} and blocking temperatures T_B found (as of May 2017). The red squares indicate lanthanide-based single molecule magnets (SMMs) and the black circles lanthanide-based single-ion magnets (SIMs). The blue hexagons Endohedral magnetic fullerene single molecule magnets (EMF-SMMs). Adapted from [20].

Figure 7 shows a highest anisotropy barrier of $U_{eff} = 1025$ K for [Dy(bbpen)Br] and a record blocking temperature of $T_B = 30$ K at a sweeping rate of 200 Oe/s for $[DyL_2(H_2O)_5]$. It is interesting to note that most of the molecules presented in Figure 7 are Dy-based. This provides a solid reason to believe in the advantages of doing research with Dy-based molecules.

[6] U_{eff} and Δ are used interchangeably in this dissertation for the anisotropy barrier.

Chapter 3. Experimental details

3.1 Sample description

Two dysprosium – based molecules were characterised in this project. Their chemical formulas are $Dy_7(EDDC)_3(ppch)(O_3PC_{10}H_7)_3(OAc)_5(MeOH)_2$, (molecule 2015 for practical purposes) and $Dy_7(\mu_3\text{-}OH)(EDDC)(spch)_4(O_3PC_{15}H_{11})_4(OAc)_2(MeOH)_4$, (molecule 2016). Molecules 2015 and 2016 were synthesised at the School of Chemistry and Chemical Engineering of Nanjing University, China. Both molecules are depicted in Figure 8:

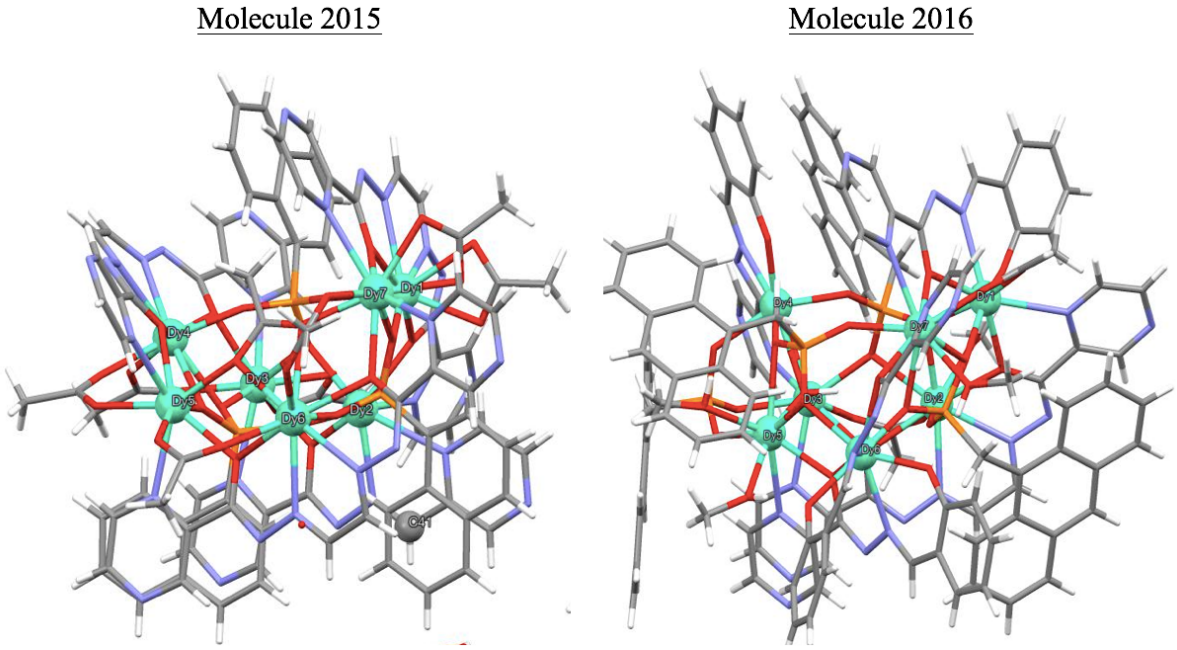

Figure 8. Molecule 2015 (left) and Molecule 2016 (right) recreated from XRD data with the programme Mercury IPS. The light blue spheres are the 7 Dy(III) ions. The grey, purple, red, orange and white sticks represent carbon, nitrogen, oxygen, phosphorus and hydrogen atoms.

As can be seen in Figure 8, both molecules are polynuclear and have complex ligand structures. However, the core of the molecules, i.e. the 7 magnetic ions and their most immediate environment are very similar in both molecules. In molecule 2015, each Dy(III) ion is bound to two Dy(III) ions via double oxygen bridges, that is, a total of 7 double-oxygen bridges. The average length of the bridges ranges between $4{,}798 - 4{,}940$ Å for molecule 2015 and $4{,}752 - 4{,}934$ Å for molecule 2016 (see Appendix to Chapter 3 , page 33). The main difference between both molecules is that molecule 2016 has an extra bond between two Dy(III) ions connected via a single oxygen bridge. Thus, molecule 2016 has a total 7 double oxygen bridges and 1 single oxygen bridge. A simplified picture of both molecules is presented in Figure 9:

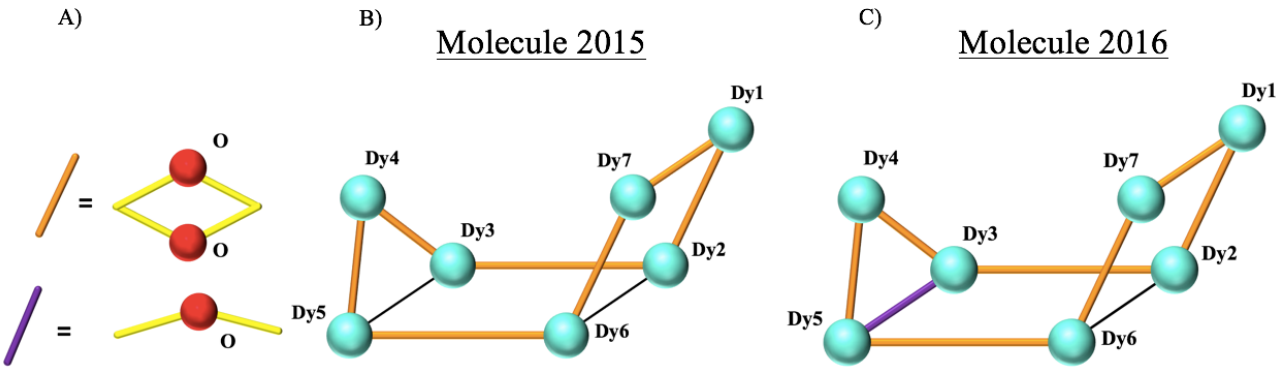

Figure 9. Reduction of both molecules to their magnetic core. A) The orange sticks represent a double oxygen bridge and the purple stick a single oxygen bridge. B) Molecule 2015 has 7 double oxygen bridges. C) Molecule 2016 has 7 double oxygen bridges and 1 single oxygen bridge between Dy_5 and Dy_3.

3.2 Sample preparation

The samples were ground for homogenisation and then introduced in capsules:

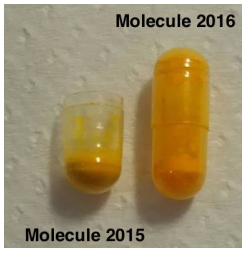

Figure 10. Samples in capsules.

Hexane was then added to the samples to prevent grain ordering at cryogenic temperatures. The capsules were then introduced in straws for the measurements in the SQUID magnetometer:

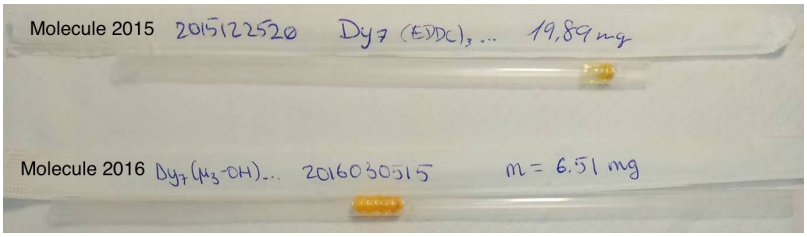

Figure 11. Capsules placed in straws for measurement. The number to the right of each straw is the sample mass. The sample mass for molecule 2015 is $m_{2015} = 19{,}89$ mg and $m_{2016} = 6{,}51$ mg for molecule 2016.

3.3 Equipment

AC susceptibility measurements as a function of frequency, temperature and DC magnetic field were performed using a Magnetic Properties Measurement System (MPMS). The precision in the susceptibility and frequency measurements is approximately 1%, and 0,45 % for the measurement of the temperature.

When the MPMS operates in DC mode, a DC magnetic field is applied to the sample. The sample is introduced in a coil which has a turn at each end of the coil and two turns in the opposite direction at the centre of the coil (see Figure 12) When the magnetic sample is swept along the entire coil it induces an electromotive force (voltage) proportional to its magnetic moment. Hence, from the analysis of the measured voltage the DC magnetic moment of the sample is calculated[7].

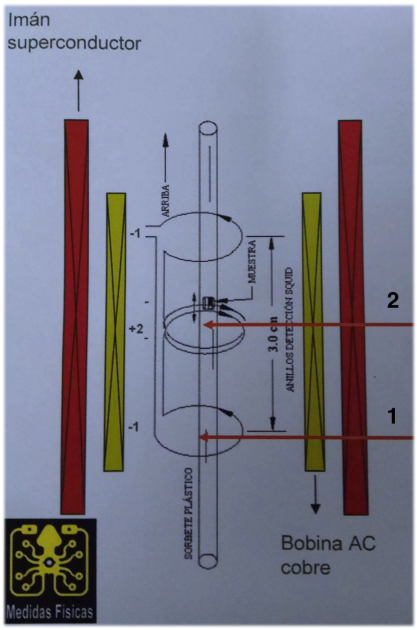

Figure 12. AC susceptibility measurement setup. DC superconducting magnet in red, additional AC coil in yellow.

In the case of the AC mode, a DC field may or may not be applied to the system. An additional excitation coil is used to apply an AC voltage and induce an AC magnetization on the sample (yellow part in Figure 12). The measurement of this AC magnetization is slightly more intricate than a DC measurement and therefore will not be described here (see Appendix to Chapter 3 , page 35 for an explanation). By performing what is known as a two-point measurement (points 1, 2 see Figure 12), the system is capable of detecting an AC magnetization signal of the sample with a resolution of $\sim 10^{-8}$ J/T (emu).

AC susceptibility measurements are necessary to characterise the relaxation processes. The volume susceptibility χ_v is related to the magnetisation and the magnetic field strength as previously seen:

$$M = \chi_v H \tag{10}$$

where χ_v is a dimensionless magnitude in SI units (emu/cm^3 in CGS units). There are two other measures of susceptibility, the mass susceptibility χ_ρ, measured in m^3/kg in SI units (emu/g in CGS units) and the molar susceptibility χ_{mol}, measured in m^3/mole in SI units (emu/mole in CGS units). The three are related by $\chi_\rho = \chi_v/\rho$ where ρ is the density of the material, and $\chi_{mol} = \chi_v/N$ where N is the number of moles of material.

In AC magnetic measurements, a small AC field $H_{AC} = H_0 \cos(wt)$ is superimposed on the DC field. This induces a time-dependent magnetisation due to the magnetic moments of the system following the alternating magnetic field:

$$M_{AC} = \frac{dM}{dH} H_0 cos\ (\omega t) \tag{11}$$

where M_{AC} is the magnetisation induced by the small AC field $H_0 \cos(\omega t)$, with frequency ω, and M is the magnetisation induced by the DC field, H. The AC susceptibility is $\chi_{AC} = dM/dH$, which

[7] The analysis of the measured voltage includes the geometry of the system: number and diameter of the turns, length of the coil, distance between turns, etc.

implies that very small variations in M can be detected even when the magnitude of M is high with respect to M_{AC}. This modelling of the AC susceptibility is valid for AC fields at low frequencies. At higher frequencies, however, the magnetic moments of the system are unable to follow the fast-changing AC field. This is, the magnetic moments become de-phased with the driving AC field. This is modelled by introducing an imaginary term in the AC susceptibility [17] so that:

$$\chi = \chi' - i\chi'' \tag{12}$$

where χ' and χ'' are the real and imaginary parts of the AC susceptibility. The imaginary part χ'' is non-zero in systems with energy dissipation processes, such as thermal relaxations. Kramers and Kronig [21] showed that real and imaginary parts are not independent of each other. The imaginary and real parts are related to the relaxation mechanisms [22]:

$$\chi' = Re\left(\chi_S + \frac{\chi_T - \chi_S}{1 + i(\omega\tau)^{1-\alpha}}\right) \quad \chi'' = Im\left(\chi_S + \frac{\chi_T - \chi_S}{1 + i(\omega\tau)^{1-\alpha}}\right) \tag{13}$$

Where i is the imaginary unit, ω is the frequency of the AC field, and τ is the relaxation time[8]. χ_T is known as the isothermal susceptibility, which represents the AC susceptibility of the system when the frequency of the driving field is low enough to allow perfect heat exchange between the spin system and the lattice. χ_S is the adiabatic value, accounting for the AC susceptibility at high AC driving frequencies, where the spin system is physically unable to exchange heat with the lattice. The term α is related to the distribution of relaxation times; when it has a value of 0, there is solely one relaxation time, the higher its value, the broader the distribution of relaxation times. Fittings of experimental data to equations (13) enable the determination of the relevant relaxation parameters τ and α.

The representation of χ'' as a function of χ' is known as a Cole-Cole plot, and takes the shape of a perfect semicircle for a single relaxation mechanism with $\alpha = 0$ [23]:

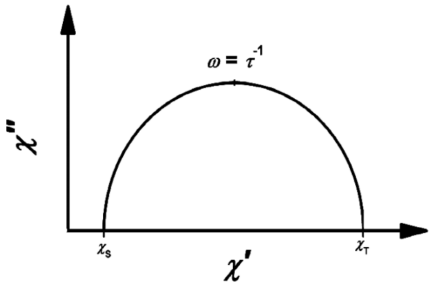

Figure 13. Cole-Cole plot for a single relaxation mechanism with $\alpha = 0$. The frequency of the highest χ'' value corresponds to the inverse of the relaxation time τ. Adapted from [23].

This process is known as a Debye process. When the distribution of relaxation times is broad, i.e. $\alpha > 0$, the Cole-Cole plot becomes a flat semicircle as will be seen in Chapter 4.

[8] If there is more than one relaxation mechanism, equations (13) must be modified, as will be seen in the next chapter.

Chapter 4. Experimental results and data treatment

4.1 DC Measurements

4.1.1 DC Susceptibility

The DC susceptibility as a function of temperature under an applied DC field of 1000 Oe was measured for both molecules to characterise their static magnetic behaviour.

The magnetic ions within a molecular magnet might interact weakly with each other. In this case, the Curie formula mentioned in Chapter 2 must be modified to account for these interactions. This problem can be treated in the molecular field approximation, which entails the addition of a perturbation term governed by a parameter, α, which gives the interaction intensity between two nearest neighbours. When this term in the Hamiltonian is considered, the Curie Law is modified to give the Curie-Weiss law see (Appendix to Chapter 4 , page 36 for the derivation [24]):

$$\chi = \frac{C}{T - \theta} \tag{14}$$

Where χ is the DC susceptibility, C the Curie constant, T the temperature, and θ the Weiss constant, which is directly proportional to the interaction strength parameter α. When α (and therefore θ), is positive, the interactions are ferromagnetic since they favour parallel alignment of the magnetic centres, whereas a negative value for α (and therefore θ) is characteristic of antiferromagnetic interactions favouring antiparallel alignment of the magnetic moments.

The Curie and Weiss parameters can be extracted from fitting the experimental data $1/\chi$ vs T to a straight line (see Figure 14A). The fit should be performed on data values of $1/\chi$ for which $T \geq 10\theta$ to ensure the validity of the Curie-Weiss law, since at lower temperatures the curvature of the curve becomes pronounced [25]. The range $T > 50$ K was used for the fitting for molecules 2016 and 2015 to ensure the validity of the Curie-Weiss law.

The Curie parameter for molecule 2016 was determined to be $C = 100{,}0 \pm 0{,}1$ emu K/mole Oe and the Weiss parameter $\theta = -3{,}46 \pm 0{,}10$ K. The uncertainties are statistical errors from the fittings. The intercept of the fitted curve with the vertical axis is above the 0 line, which is the reason θ has a negative value. This implies weak antiferromagnetic interactions. This can be verified when plotting χT vs T (see Figure 14B), which yields a curve characteristic of antiferromagnetic interactions [24]. Qualitatively, when the system is at high T, the magnetic moments are uncorrelated since the thermal energy is much larger than the interaction energy.

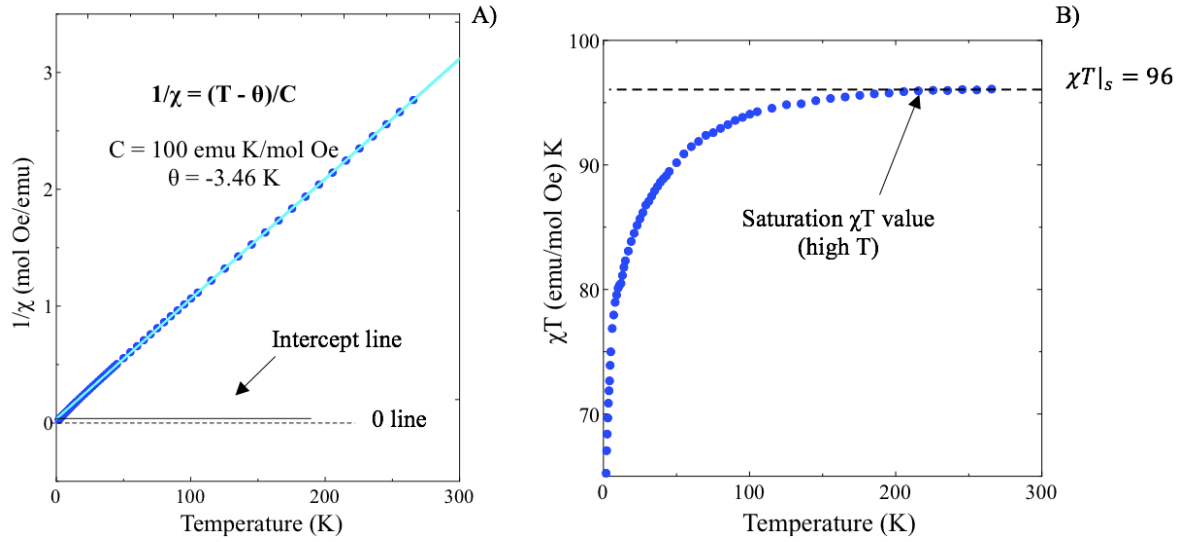

Figure 14. Molecule 2016. A) $1/\chi$ vs T for $H_{DC} = 1000$ Oe. The solid line is the fit of the Curie-Weiss formula to the experimental data. The fitted curve intercepts above the 0 line with the vertical axis, leading to a negative value for θ. B) χT vs T indicates antiferromagnetic behaviour. The saturation value for $\chi T|_s$ can be extracted from the high temperature data.

However, when the thermal energy decreases, interactions dominate, leading to antiferromagnetic configurations and a decrease in χ.

From the high temperature limit, where the magnetic moments are independent of each other, the effective magnetic moment is obtained from the Curie Law:

$$\chi T|_s = \frac{N\mu_{\text{eff}}^2}{3k_B} \tag{15}$$

The saturation value for $\chi T|_s$ is $96{,}0 \pm 1{,}3$ emu K/mole Oe, where the uncertainty has been calculated by taking into account the precision of the equipment. (See Figure 14B). By taking $N = 6{,}022 \times 10^{23}$ mole^{-1} (Avogadro's constant), Boltzmann's constant $k_B = 1{,}38 \times 10^{-23}$J/K, and converting all parameters to the same unit system, the following value is obtained:

$$\mu_{\text{eff}} = (10{,}47 \pm 0{,}15)\,\mu_B$$

where the uncertainty has been calculated by propagating the uncertainty for $\chi T|_s$.

The theoretical value for the magnetic moment of a free Dy (III) ion is calculated using [17]:

$$\mu_{eff} = g_J \mu_B \sqrt{J(J+1)} \tag{16}$$

where $g_J = 4/3$ is the gyromagnetic factor ($S = 5/2$ $L = 5$ $J = 15/2$ for Dy(III)). The theoretical value is:

$$\mu_{\text{eff}}|_{theo} = 10{,}64\,\mu_B$$

The experimental value is in very good agreement with the theoretical value (98,4 % of the theoretical value).

Molecule 2015 displays a somewhat different behaviour (see Figure 15A). Firstly, the intercept of the fitted curve with the vertical axis is below 0, implying ferromagnetic interactions, $\theta = 2{,}14 \pm 0{,}41$ K. This can be seen at high temperature ($T > 80$ K) in the χT curve (see Figure 15B). The value for the Curie constant is: $C = 85{,}5 \pm 0{,}2$, similar to molecule 2016.

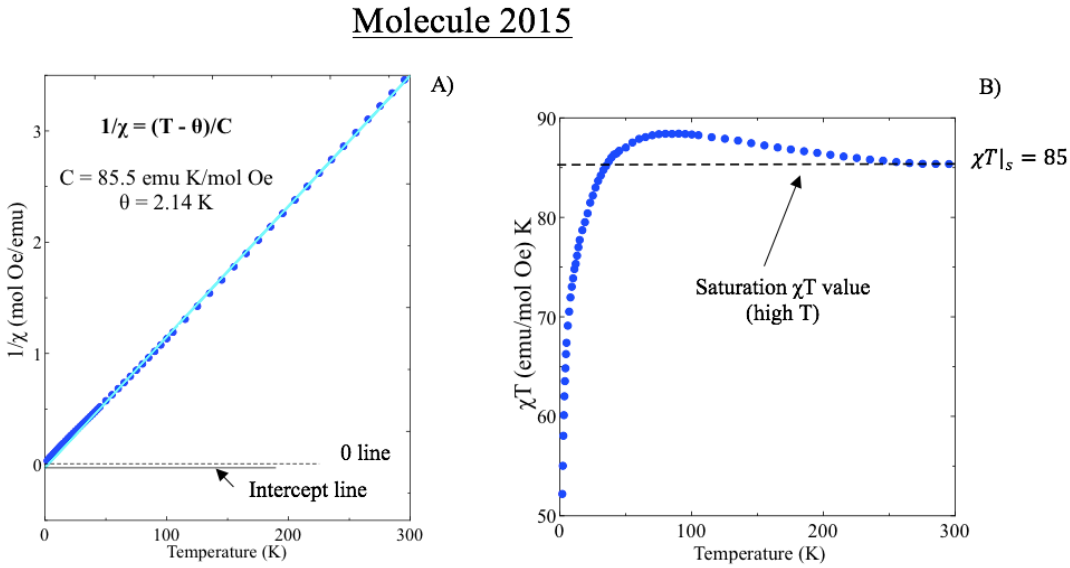

Figure 15. Molecule 2015. A) Fit of the Curie-Weiss formula to the experimental data for $H_{DC} = 1000$ Oe. The fitted curve intercepts below the 0 line with the vertical axis, leading to a positive value for θ. B) The tendency indicates ferromagnetic behaviour. The saturation value for $\chi T|_s$ can be extracted from the high temperature data.

However, at lower temperatures, the molecule presents antiferromagnetic interactions akin to those seen in molecule 2016. The Curie-Weiss law was fitted to the experimental data at high temperatures, which is why the sign of θ indicates a ferromagnetic behaviour despite the system having both ferromagnetic and antiferromagnetic behaviours. Molecule 2016 might have ferromagnetic interactions at high temperature and antiferromagnetic interactions at lower temperatures due to different energy levels being populated at different temperatures [24].

The effective magnetic moment is calculated from the saturation value of $\chi T = 85{,}0 \pm 1{,}2$ emu K/mole Oe, yielding:

$$\mu_{\text{eff}} = (9{,}89 \pm 0{,}14)\ \mu_B$$

which is slightly below the value obtained for molecule 2016. Nevertheless, this value is 93% of the theoretical value. The reason for having discrepancies for both molecules with respect to the theoretical calculation might be that 300 K might not be the "high temperature limit" for neither molecules. In fact, it can be seen in (see Figure 15B) that χT for molecule 2015 has barely started to saturate.

4.1.2 Magnetisation

The DC magnetisation curves, M(H), of the molecules was measured at T = 1,8 K. The magnetisation data was converted from emu to number of μ_B (Bohr magneton):

$$M(emu) \rightarrow M(\mu_B) = M(emu)\frac{Mm(g/mol)}{N_A(mol^{-1})M(g)\,\mu_B}$$

where $M(\mu_B)$ is the magnetisation in number of μ_B, Mm(g/mol) is the molecular mass of the molecule, N_A is Avogadro's number and M(g) is the sample mass of the molecule in grams. The benefit of using number of μ_B is that the magnetisation is independent of the number of moles of sample.

A simulation programme (MAPGPACK) was used to obtain a theoretical model of the Dy system at 1,8 K. It was designed by J. J Borrás-Almenar et al. from the Inorganic Chemistry department at the University of Valencia [26].

Briefly, the programme solves the Hamiltonian of the system considering the interaction of the magnetic centres with their environment (crystal field), the interaction of the magnetic moments with the applied magnetic field (Zeeman interaction) and the interaction between magnetic centres (exchange interaction). The solutions of the Hamiltonian are then used to calculate the partition function. Next, the partition function is used to calculate the magnetisation, susceptibility and/or the heat capacity.

There are 7 magnetic centres in both molecules, corresponding to the 7 Dy(III) ions. Since Dy(III) is a Kramers ion, the energy levels are split into doublets. At low temperatures, only the ground state is populated in Dy since the next energy level is usually dozens of Kelvin above the ground state [27]. As a consequence, the ion is considered to be an effective $S' = 1/2$ spin system since there are only two available energy levels [24].

- **Molecule 2015**

Other input parameters are the magnetic exchange constants between the ions, and the anisotropy tensors of each ion, which carry the information of the environment of the magnetic centres (crystal field). In the previous section, it was seen that at T = 1,8 K the interactions between the ions are antiferromagnetic (even though ferromagnetic behaviour at higher temperatures was observed). Therefore, all the input exchange constants were set at negative values. The best fit corresponds to $\alpha_{ij} = -0{,}6$ K for all Dy(III) pairs i, j (see Figure 16).

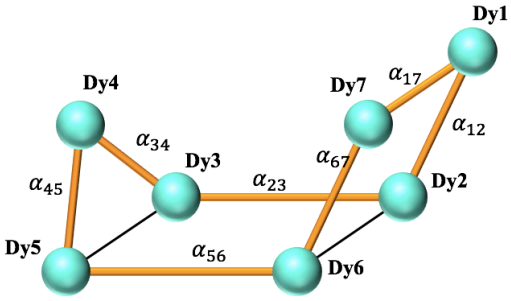

Figure 16. Magnetic core of molecule 2015. α_{ij} is the exchange parameter between Dyi and Dyj.

The interaction of the magnetic field with the effective spin of the ions is given by the anisotropy tensor (g-tensor) and is described in the Appendix to Chapter 4 , page 31. The estimation of the matrix elements for the anisotropy tensors is somewhat more tedious, reason being the asymmetric nature of the molecule. Ab initio calculations of Dysprosium-containing molecules found in the literature usually yield: $g_z \approx 19-20, g_x = g_y \approx 0$ and 0 for the off-diagonal components [28,29] due to symmetry considerations and the right coordinate system. In molecule 2015, the asymmetry means none of the matrix elements are necessarily 0 for each of the 7 Dy(III) ions.

A toy model for molecule 2015 was made to ease the prediction of the anisotropy directions (given by the g-tensors) for each Dy(III) ion (see Figure 17B). Chilton et al. [29] developed an electrostatic model to calculate the g-tensors of high-symmetry molecules, including a Dy_6 ring with a very similar environment of the ions to that of molecules 2015 and 2016 (see Figure 18). Their results were used as a basis for the prediction of the anisotropy axes for molecule 2015 given the similarity between the environment of the magnetic centres in their molecules and molecule 2015 (Figure 17C):

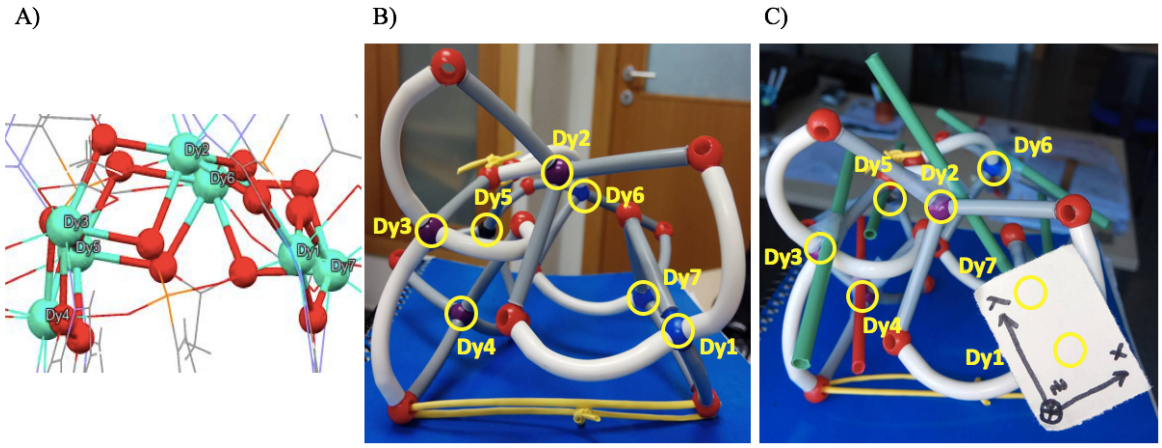

Figure 17. A) View of molecule 2015 recreated from XRD experiments. B) Toy model of molecule 2015. The yellow strings at the bottom provide the torsion of the molecule. C) Toy model of molecule 2015 with estimated anisotropy axes (green and red bars). The z axis is chosen as the direction of the anisotropy axis of Dy_1. The x and y axes have been chosen as shown in the white paper.

The results presented by Chilton et al. implied a disposition of the anisotropy axis as in Figure 18:

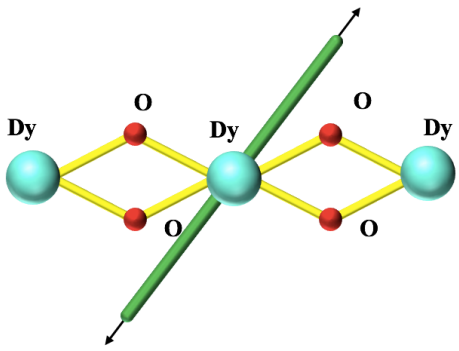

Figure 18. Estimation of the anisotropy axis (green bar) based on the results by Chilton et al [28,29]. The black arrow indicates the direction of the anisotropy axis. The light blue spheres represent Dy(III) ions, bound together by double oxygen bridges (red spheres). Indeed, the connection between Dy ions is via double oxygen bridges, like in molecules 2015 and 2016.

The g-tensors must be expressed in terms of a basis. The direction of the anisotropy axis for Dy_1 was chosen as the z axis (see Figure 17C) and the y and x axes were chosen as seen in the figure. Thus,

the expression for the g-tensors of the other 6 Dy(III) ions must be transformed via rotation matrices in the following manner [18]:

$$g' = R(\alpha, \beta, \gamma)\, g\, R^{-1}(\alpha, \beta, \gamma) \tag{17}$$

where g' is the transformed g-tensor, $R(\alpha, \beta, \gamma)$ is the rotation matrix around the axis defined by the Euler angles α, β, γ and R^{-1} is its inverse.

The rotation matrices $R(\alpha, \beta, \gamma)$ were calculated by estimating the angles that defined them (α, β, γ), which were the angles the anisotropy axes formed with the x, y and z axes. Operations were performed on the g-tensors (see Table A4 Appendix to Chapter 4 , pages 37, 38).

Table A4 shows the g-tensor for the Dy_1 ion has only a component in the z direction, as chosen. Also, all the other Dy(III) ions have non-zero off-diagonal elements. This brings about a problem due to the limitation of the programme used for the simulation; the programme only allows for the components g_{xx}, g_{yy}, g_{zz} as inputs. Therefore, not all the information of the molecule can be transferred to the programme for the simulation. However, the simulation was considerably good when comparing to the experimental data (Figure 19):

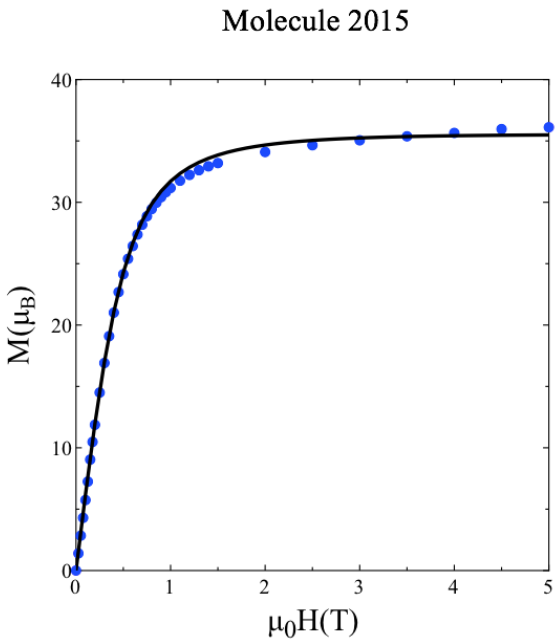

Figure 19. Molecule 2015. Experimental (blue dots) and simulated (black line) magnetisation curves at T = 1,8 K. The input parameters included the calculated g-tensor diagonal for each ion, exchange constants $\alpha = -0{,}6$ K for all ion pairs and a magnetic field at a 20° angle with the defined z axis.

The simulation inputs are the diagonal of the g-tensors, $\alpha = -0{,}6$ K for all ions and a magnetic field applied at a 20° angle with respect to the z axis.

The simulation exhibits an early saturation at 2 T, where the experimental curve does not present saturation in the measured magnetic field range. This discrepancy is attributed mainly to not taking into account the off-diagonal elements in the simulation. Other sources of uncertainties include the inaccuracy of the estimated anisotropy axis presented in the toy model. In fact, it was observed that very slight variations in the rotation matrix angles used to calculate the g-tensors produced significant

changes in the g-tensors and consequently in the magnetisation curves (see Appendix to Chapter 4 , page 38).

- **Molecule 2016**

Due to the similarity between both molecules, the g-tensor used for molecule 2015 was used for molecule 2016 as a first approximation. The best-fit exchange parameters were observed to be $\alpha = -0{,}9$ K for all ions pairs. The extra bridge from Dy_3 to Dy_5 (see Figure 20) was included in the simulation.

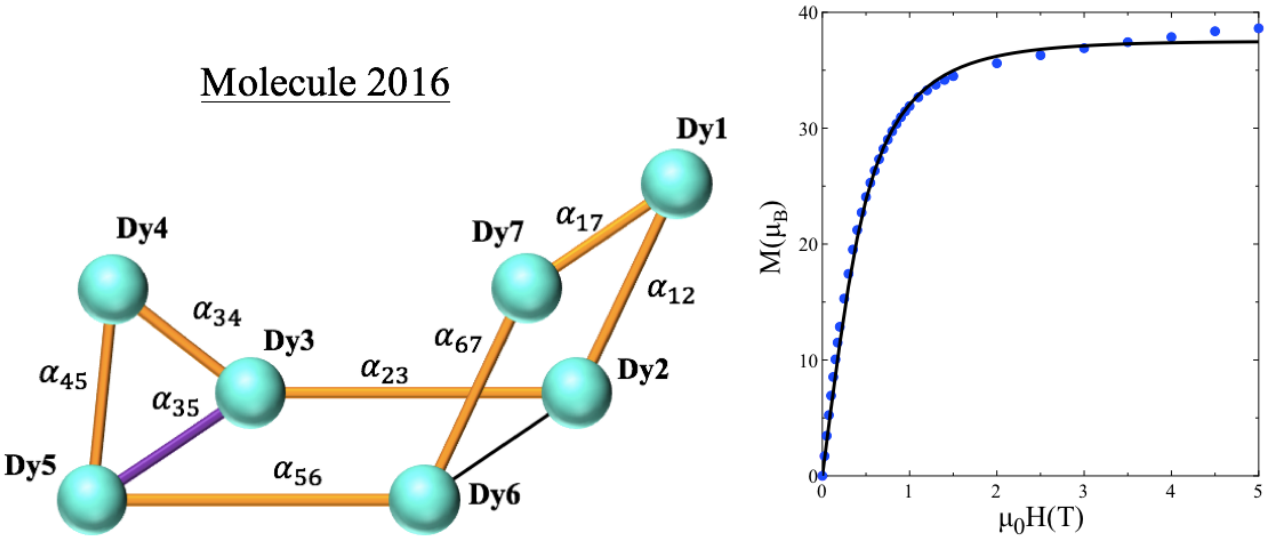

Figure 20. Left: magnetic core of molecule 2016. The extra interaction parameter α_{35} between Dy_3 and Dy_5 was included in the simulation. Right: Simulation of M(H) (black line). The input parameters were: diagonal elements of the g-tensor calculated for molecule 2015, $\alpha = -0{,}9$ K for all ion pairs and a magnetic field applied along the z axis.

The simulation represents the experimental data considerably well. The discrepancies are attributed mainly to the exclusion of the off-diagonal elements of the g-tensor for each Dy(III) ion.

The M(H) curves for both molecules were observed to be very similar (see Figure A4 in Appendix to Chapter 4, page 38), as expected from their almost-identical chemical structures.

4.2 AC Susceptibility measurements

AC susceptibility measurements at different frequencies, temperatures and DC fields were performed to characterise the dynamic magnetic behaviour of both molecules.

The raw data consisted of two sets of measurements. The first set: magnetisation measurements at different frequencies $\omega = 0{,}08 - 1400$ Hz, for several DC magnetic fields $H_{DC} = 0 - 10000$ Oe at $T = 1{,}8$ K. The second, magnetisation measurements at different frequencies $\omega = 0{,}08 - 1400$, at a fixed field (different for each molecule), at different temperatures $T = 1{,}8 - 6.63$ K. The first step was to convert the magnetisation data to susceptibility:

$$M_{AC}(\omega, H_{DC}, T = 1{,}8\ K) \rightarrow \chi_{AC}(\omega, H_{DC}, T = 1{,}8\ K) = \frac{M_{AC}(\omega, H_{DC}, T = 1{,}8\ K)}{\mu_0 H_{AC}}$$

4.2.1. Molecule 2016

As discussed in Chapter 2, χ_{AC} has real and imaginary components: χ', χ'', respectively. A plot of χ'' as a function of χ' (Cole-Cole plot discussed in Chapter 3), was drawn for different fields with the experimental data because it provides information about the relaxation mechanisms [22] (see Figure 21):

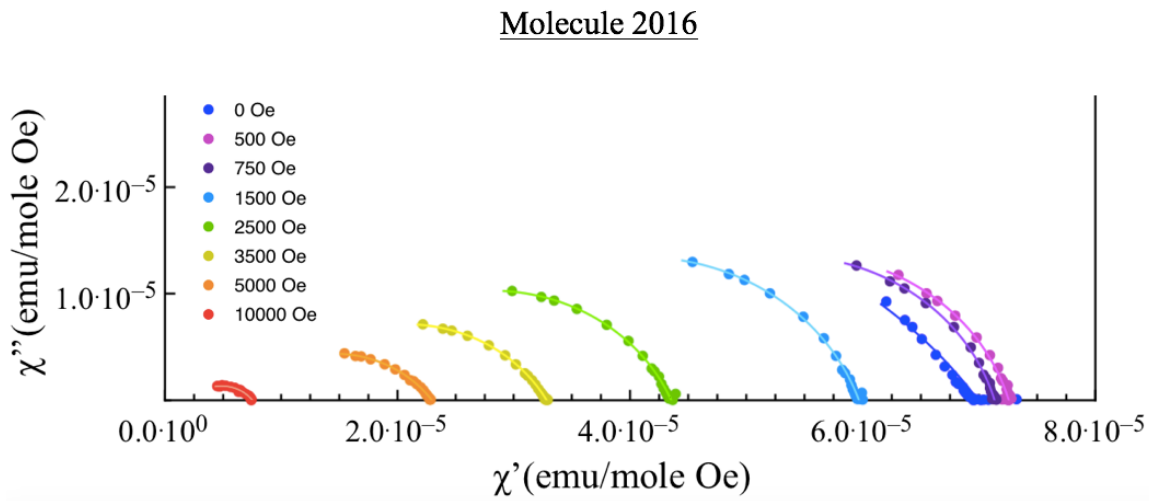

Figure 21. Molecule 2016. Cole-Cole plots for different magnetic fields; 0-10000 Oe at T = 1,8 K. The solid lines are the fitted curves. The 500 Oe curve is shifted to the right of the zero-field data. Higher fields are shifted to the left with respect to the 500 Oe curve.

The shape of the experimental curves implied there was one relaxation mechanism (only one semicircle) and thus χ' and χ'' were fitted to the following formulae:

$$\chi' = Re\left(\chi_S + \frac{\chi_T - \chi_S}{1 + i(\omega\tau)^{1-\alpha}}\right) \quad \chi'' = Im\left(\chi_S + \frac{\chi_T - \chi_S}{1 + i(\omega\tau)^{1-\alpha}}\right) \qquad (18)$$

Where χ_T is the isothermal (or low-frequency) susceptibility, χ_S is the adiabatic (or high-frequency) susceptibility, τ is the relaxation time and α is the Cole-Cole parameter.

As can be seen in Figure 21, the curve representing the 500 Oe data is shifted to the right of the zero-field curve. Higher fields are shifted to the left of the 500 Oe curve. The curves describe an incomplete semicircle; high-frequency data would be necessary to yield the entire semi-circle representing the relaxation mechanism. However, the available data suffices to provide good fits.

An upward tail at the right of each curve can be intuited for some fields (1500 and 2500 Oe), which might indicate the existence of a second relaxation mechanism in the lower frequency range (low frequencies for high values of χ'). However, despite attempts to fit to two relaxation mechanisms, the

fittings for one relaxation mechanism outdid the fittings for two relaxation times in terms of mapping the shape of the experimental data (see Figure A5 in Appendix to Chapter 4 page 39).

The curves are flat semi-circles, especially at higher frequencies, which indicates a distribution of relaxation times for the relaxation mechanism [23]. Table A5 in Appendix to Chapter 4 , page 36 shows the fitted values for the relaxation parameters τ and α and their fitting errors for different DC fields. As can be seen in the table, the Cole-Cole parameter α does indeed increase with the applied magnetic field, implying a broadening of the distribution of relaxation times with the DC field. This means that different contributions to the magnetisation relax with slightly different relaxation times (see Table A5 in Appendix to Chapter 4 , page 40).

This last claim is true except for the zero-field data. However, the fit to this particular data set is thought to be the poorest out of all, reason being the data points to the right end of the zero-field curve (navy blue curve Figure 21). This might also explain the relatively low relaxation time and high uncertainties for this curve in comparison to the non-zero-field data.

The relaxation times indicate a quick relaxation mechanism: $\tau = 0{,}048 - 1{,}157$ ms. The nature of the relaxation process must be determined evaluating the variation of the relaxation time with the DC field and/or the temperature (the latter is used in this project). Quantum tunnelling relaxation is excluded since it involves relaxation times several orders of magnitude below the obtained, and therefore thermal relaxation via Orbach, Raman or Direct processes is expected. To assess the nature of this relaxation mechanism, AC susceptibility measurements were performed at a fixed field $H_{DC} = 1500$ Oe for different temperatures (see Figure 22):

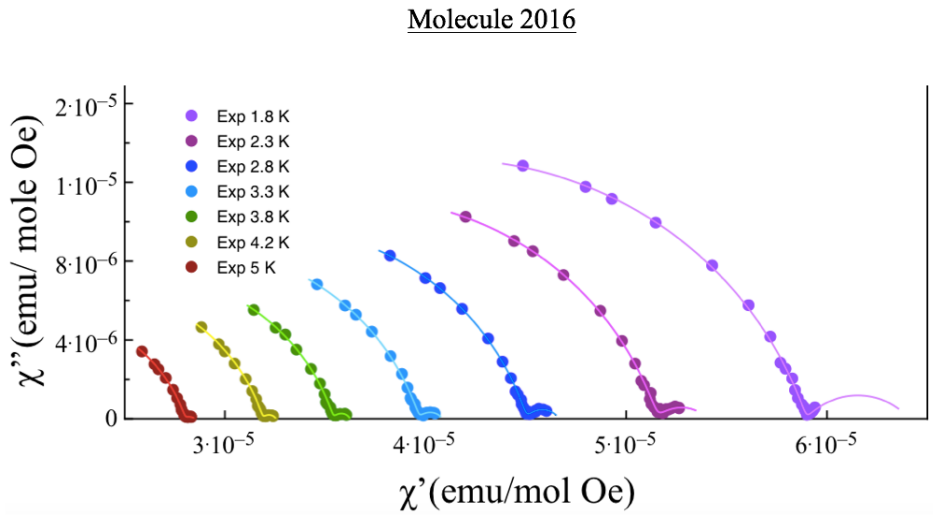

Figure 22. Cole-Cole plots at a constant DC field $H_{DC} = 1500$ Oe for various temperatures. The solid lines are the fittings to equations (19). A second, minor relaxation mechanism can be observed at the high χ' side of each curve.

As can be seen in the figure, both the real and imaginary susceptibility decrease with increasing temperature (Curie-Weiss law). Also, a minor, second relaxation mechanism appears at the high χ' side of each curve. The term "minor" refers to the fact that only a small fraction that contributes to

the magnetisation relaxes with the second relaxation mechanism. A second relaxation mechanism was not observed for the previous set of AC susceptibility measurements at $H_{DC} = 1500$ Oe and T = 1,8 K. Nevertheless, the main relaxation mechanism is the same as observed in the AC susceptibility data as function of DC field. The fitted relaxation parameters are presented in Table A6 Appendix to Chapter 4 page 40.

The Cole-Cole parameter remains constant throughout the temperature range, meaning the distribution of relaxation times does not depend on the temperature for T = 1,8 - 5 K. To identify the relaxation mechanism, the variation of the relaxation time with the temperature must be evaluated (Figure 23):

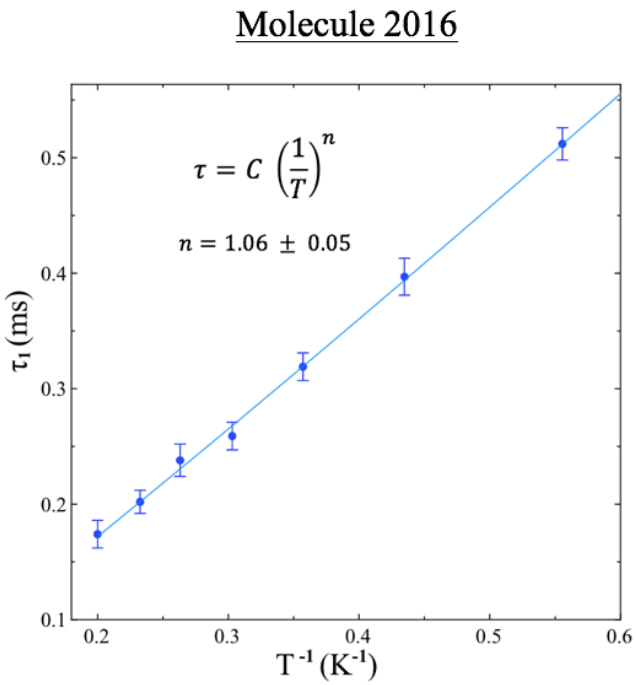

Figure 23. Molecule 2016. Fit of τ_1 vs 1/T to determine the relaxation mechanism. The fitting to a straight line (light blue) yields a value $n = 1.06 \pm 0.05$, which is considerably close to 1, indicating a direct process [17]. The error bars were used for the fitting.

The data was fitted considerably well to a straight line when plotting $\tau_1 \text{vs} \left(\frac{1}{T}\right)$, indicating a linear dependence of the relaxation time with the inverse of the temperature, which is characteristic of a direct relaxation process [17]. As can be seen in Figure 22, the AC susceptibility data was fitted to account for two relaxation mechanisms, and therefore the formulae mentioned earlier (equations 18), had to be modified accordingly by changing the code of the fitting programme [23]:

$$\chi' = Re\left(\chi_{S1} + \chi_{S2} + \frac{\chi_{T1} - \chi_{S1}}{1 + i(\omega\tau_1)^{1-\alpha_1}} + \frac{\chi_{T2} - \chi_{S2}}{1 + i(\omega\tau_2)^{1-\alpha_2}}\right)$$
$$\chi'' = Im\left(\chi_{S1} + \chi_{S2} + \frac{\chi_{T1} - \chi_{S1}}{1 + i(\omega\tau_1)^{1-\alpha_1}} + \frac{\chi_{T2} - \chi_{S2}}{1 + i(\omega\tau_2)^{1-\alpha_2}}\right) \quad (19)$$

Where χ_{S1}, χ_{T1}, τ_1, and α_1 are the adiabatic and isothermal susceptibilities, the relaxation time and the Cole-Cole parameter of one relaxation mechanism respectively, while the namesake parameters labelled 2 correspond to the second relaxation mechanism. A second term was added to account for a second relaxation time, as described in [23].

The second, minor relaxation time was also characterised (Figure 24):

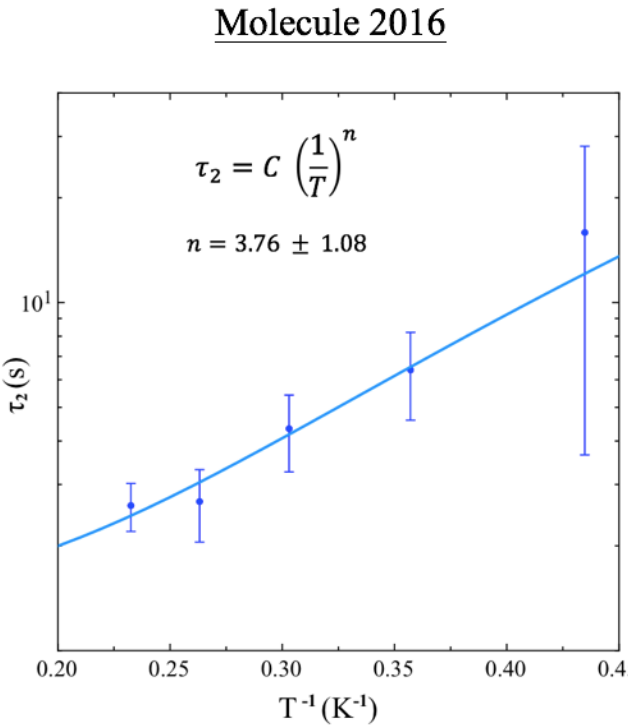

Figure 24. Molecule 2016. Fit of τ_2 vs $1/T$ to determine the relaxation mechanism. The fitting to a straight line (light blue) yields a value $n = 3.76 \pm 1.08$, which lies between $2 \leq n \leq 4$, characteristic of a bottlenecked Raman effect [30]. The error bars, obtained from the Cole-Cole fittings as a function of temperature were used for the fitting.

This relaxation mechanism is slower than the previous characterised: $\tau_2 = 2{,}6 - 15{,}9$ s, compared to $\tau_1 = 0{,}048 - 1{,}157$ ms. The figure shows a dependence of the relaxation time: $\tau_2 \propto \left(\frac{1}{T}\right)^n$, where $n = 3{,}76$. This is characteristic of a Raman relaxation mechanism, with a slight "bottleneck effect" contribution, where $2 \leq n \leq 4$ is observed [30].

The "Bottleneck effect" occurs at low temperatures when the thermal conductivity between the spin system and the helium bath is poor. As a consequence, phonons are unable to transfer energy from the spin system to the bath fast enough to induce thermal equilibrium, which causes warming up of the lattice [17,31].

This result is questionable since the uncertainties in the fittings in Figure 24 are substantial. The reason for this is the lack of data needed to yield good fittings to the Cole-Cole curves as a function of temperature (Figure 22). For instance, the data for the 1,8 K curve (purple curve) in Figure 22 seems to only draw a small fraction of the theoretical relaxation semicircle, leading to considerably large uncertainties in these fittings. A similar, perhaps smaller effect, is observed for higher temperatures.

4.2.2. Molecule 2015

Cole-Cole plots as a function of DC field and T = 1,8 K were drawn for molecule 2015 (Figure 25):

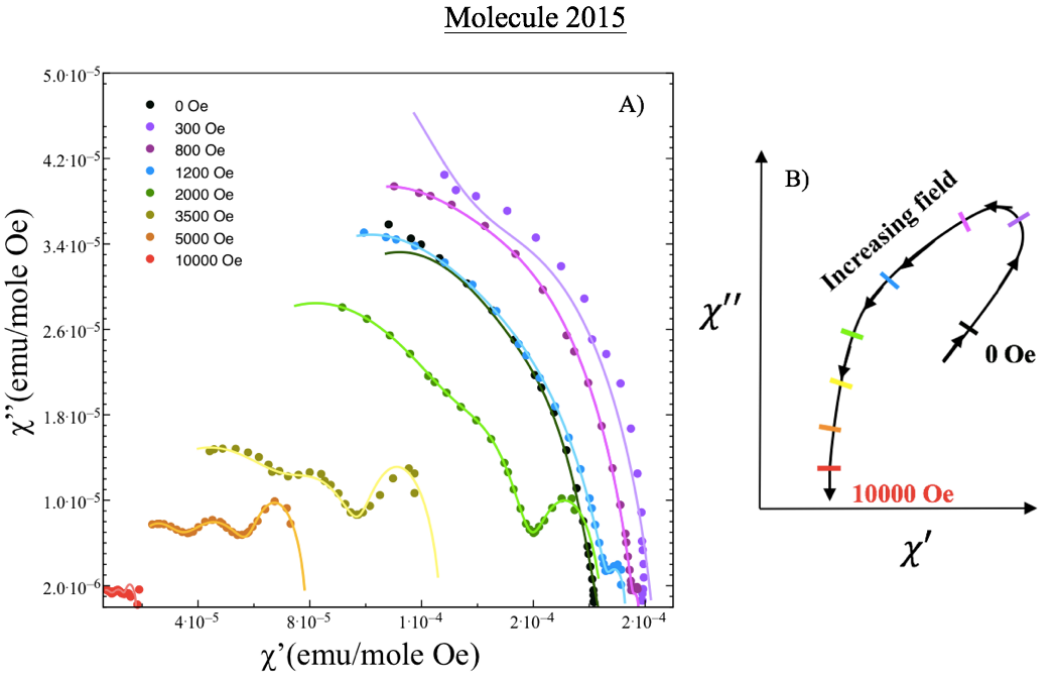

Figure 25. A) Cole-Cole plots for different magnetic fields; 0-10000 Oe at T = 1,8 K. The solid lines are the fitted curves. Two relaxation mechanisms were fitted to the 0-300 Oe data. Between 300 and 800 Oe, a third relaxation channel is opened. B) The figure represents the shift direction of the data as a function of DC field; the 300 Oe data Cole-Cole plot shifts to the right with respect to the zero-field data. Further increasing the field leads to shifting of the curves to the left of the 300 Oe data.

The data is visibly different from that of molecule 2016. From Figure 25, the 300 Oe data is shifted to the right with respect to the zero-field curve. Increasing the field leads to curves shifted to the right with respect to the 300 Oe data. The zero-field and 300 Oe-field curves were, at first, fitted to equations (18), which account for one relaxation mechanism, but later were fitted to equations (19), rendering a better agreement with the experimental data. The 800 Oe curve presented a small aggregation of data points at the right end of the curve, which was later observed to be the birth of a third relaxation mechanism. This was confirmed by fitting the data to an extension of equations (19) by modifying the code of the fitting programme, which read:

$$\chi' = Re\left(\chi_{S1} + \chi_{S2} + \chi_{S3} + \frac{\chi_{T1} - \chi_{S1}}{1 + i(\omega\tau_1)^{1-\alpha_1}} + \frac{\chi_{T2} - \chi_{S2}}{1 + i(\omega\tau_2)^{1-\alpha_2}} + \frac{\chi_{T3} - \chi_{S3}}{1 + i(\omega\tau_3)^{1-\alpha_3}}\right)$$

$$\chi'' = Im\left(\chi_{S1} + \chi_{S2} + \chi_{S3} + \frac{\chi_{T1} - \chi_{S1}}{1 + i(\omega\tau_1)^{1-\alpha_1}} + \frac{\chi_{T2} - \chi_{S2}}{1 + i(\omega\tau_2)^{1-\alpha_2}} + \frac{\chi_{T3} - \chi_{S3}}{1 + i(\omega\tau_3)^{1-\alpha_3}}\right) \quad (20)$$

Where χ_{S1}, χ_{T1}, τ_1, and α_1 are the adiabatic and isothermal susceptibilities, the relaxation time and the Cole-Cole parameter of one relaxation mechanism respectively, while the namesake parameters labelled 2 and 3 correspond to the second and third relaxation mechanisms, respectively.

It is interesting to note that the relaxation pathway that appears between 300 and 800 Oe becomes the dominant, main relaxation mechanism above 3500 Oe. From Figure 25, it can be intuited that this relaxation mechanism is the slowest, i.e. has the longest relaxation time τ_3. This is because the frequency at which the relaxation peak occurs is associated to the inverse of the relaxation time, and in Cole-Cole plots, low frequencies rest at high χ' values. Thus, since this third relaxation mechanism, with relaxation time τ_3, appears at the right of each Cole-Cole plot, it is therefore the slowest relaxation mechanism. This is verified with the fitted parameters presented in Table A7 Appendix to Chapter 4 , page 40:

In all three relaxation times, the values increase with increasing field and reach a maximum for a field value of 2000-3500 Oe, and then decrease. The Cole-Cole parameters for each relaxation pathway are presented in Table A8 Appendix to Chapter 4 page 41.

The Cole-Cole parameter for the slow relaxation pathway, α_3, is small for most fields, implying a narrow distribution of relaxation times for this relaxation mechanism. The fittings provide larger Cole-Cole α_1, α_2 values on average, but there is no clear dependence with the DC field.

AC susceptibility measurements for different temperatures at a fixed field $H_{DC} = 5000$ Oe were performed to characterise the relaxation mechanisms (Figure 26):

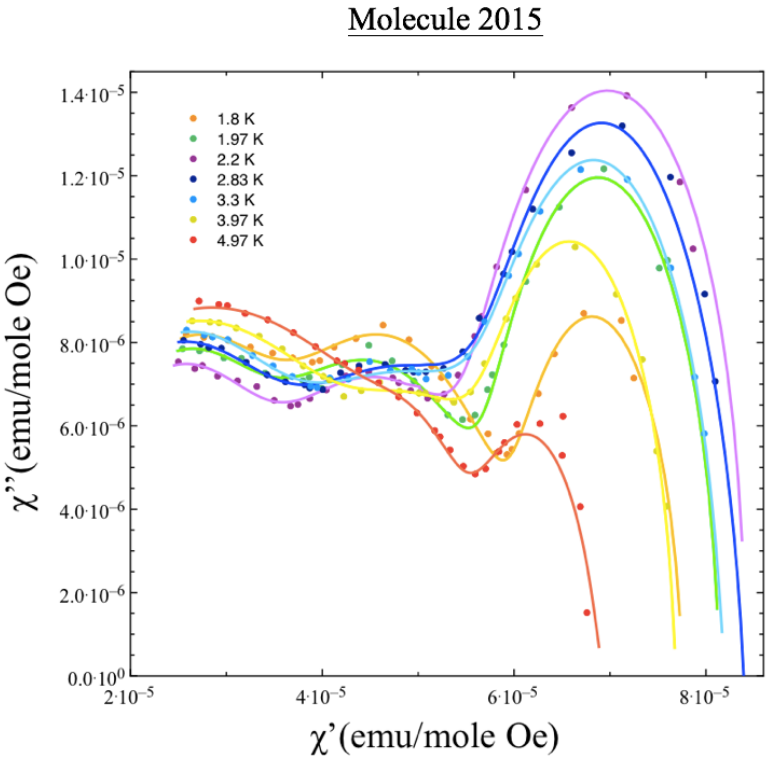

Figure 26. Molecule 2015. Cole-Cole plots for different temperatures at a fixed field $H_{DC} = 5000$ Oe. The height of the third peak (slowest relaxation mechanism) increases from 1,8 K to 2.2 K but then starts decreasing down to its lowest height at 4.97 K. Two data curves were not plotted for clarity.

Figure 26 shows that the slow relaxation mechanism is the main relaxation pathway throughout the measurement temperature range. The height of the third peak (slowest relaxation mechanism) increases from 1,8 K to 2,2 K but then starts decreasing down to its lowest height at 4,97 K. The second relaxation channel (middle peak in the curves) starts to vanish at around 3,97 K, and at 4,97 K only a mild "shoulder" can be intuited. The fitted parameters and their uncertainties are presented in Table A9 Appendix to Chapter 4 page 41.

The relaxation time τ_1 stays fairly constant throughout the temperature range; within 25 % of the average value. τ_2 varies in a random pattern whereas τ_3 decreases. The dependence of τ_3 with the inverse of the temperature is displayed in Figure 27:

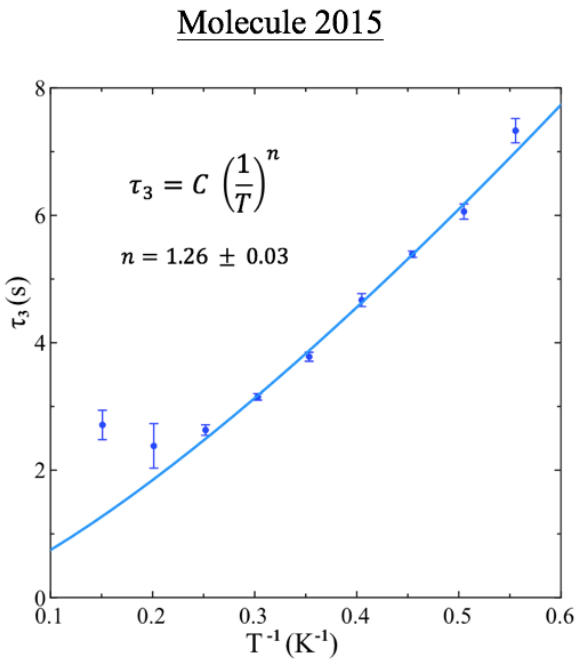

Figure 27. Plot of τ_3 as a function of the inverse of T. The fitting yields a value of $n = 1{,}26 \pm 0{,}03$, implying direct relaxation process which might have a slight bottleneck contribution. All data points and error bars were used for the fitting.

A value of $n = 1{,}26 \pm 0{,}03$ is extracted from the fitting, which is characteristic of a direct relaxation process which might have a slight bottleneck contribution since a pure direct process would yield $n = 1$ and a direct bottlenecked process $n = 2$ [17]. It is relevant to note that the experimental data provided a good fit to an Orbach relaxation process, however it yielded an energy barrier of ~ 3 K, whereas it is well known that anisotropy barriers for Dy-containing SMMs are of $\sim 25 - 330$ K and even higher values such as $842 - 1025$ K [6,32,33].

Despite some effort in attempting to fit the variation of both relaxation times τ_1, τ_2 with T to characteristic tendencies of well-known thermal relaxation processes, no trends were found. This might be due to several reasons, such as insufficiency of data points to provide good fits, and/or the mixing of various relaxation processes involved in the relaxation times.

Chapter 5. Conclusions, discussion and future work

5.1 Summary

The following conclusions can be drawn of the results:

- Molecule 2016 show antiferromagnetic interactions at low temperatures whereas molecule 2015 show ferromagnetic interactions from room temperature down to 80 K, and antiferromagnetic interactions below this temperature.
- The effective magnetic moment of the Dy(III) ion was calculated to be within 98,4% of the theoretical value for molecule 2016 and 93 % for molecule 2015.
- The magnetisation of molecules 2015 and 2016 was effectively simulated by predicting anisotropy axes on a toy model and by analogy with a somewhat similar molecular environment described in the literature. It has been proposed that the correct treatment of the molecule entails the use of the entire g-tensor, as opposed to solely its diagonal like in symmetric molecules.
- Molecule 2016 presents 2 relaxation mechanisms at low temperature: a major direct process ($\tau_1 = 0{,}048 - 1{,}15$ ms) and a minor, Raman bottlenecked, slower relaxation process ($\tau_2 = 2{,}6 - 15{,}9$ s), at $T = 1{,}8$ K.
- Molecule 2015 presents 3 relaxation pathways at low temperature. Pre-existing fitting formulae had to be extended to account for the 3 relaxation mechanisms. Out of the three relaxation pathways, the slowest ($\tau_3 = 4{,}27 - 8{,}36$ s) was determined to be a direct, slightly bottlenecked relaxation process, at $T = 1{,}8$ K.

5.2 Discussion

As mentioned throughout the dissertation, the aim of the field is to achieve magnetic molecules with high anisotropy barriers to the reversal of the magnetic moment and thus yield high relaxation times as well as accessible hysteresis (blocking) temperatures.

The utility of a magnetic molecule is determined by its properties, but also by the potential application. Molecule 2015 presented a slow relaxation mechanism of $\tau_3 = 4{,}27 - 8{,}36$ s at $T = 1{,}8$ K, which would, in principle, be useful for applications which operated in nanoseconds, microseconds, or even milliseconds. For instance, good quantum computing candidates operating as

qubits achieve highest relaxation times of several milliseconds, as discussed by Jenkins et al. [34]. On the other hand, long-term memory storage such as hard disks would not seem a plausible application; relaxation times of tens of years would be paramount.

On the other hand, it would be useful to code a programme similar to the one used for the simulations of M(H) that allowed for a correct representation of the g-tensors for each magnetic ion.

Finally, it is interesting to see such different magnetic behaviour (especially AC dynamic behaviour) in both molecules given their almost-identical structures. Understanding the correlation of the chemical structure of a molecule with its magnetic properties seems crucial in the design of molecular magnets with good magnetic properties, and therefore more research should be done to understand these correlations.

5.3 Future work

It would be interesting to perform AC susceptibility measurements at lower temperatures (below 1,8 K) to achieve a complete characterisation of the molecules and for the potential publication of the results. Also, measurements at higher frequencies would be useful to map the entire relaxation curves and minimise fitting uncertainties, hence obtaining more accurate values of the relaxation parameters.

Low-temperature measurements (below 1,8 K) can be carried out using a dilution fridge. Another part of this project was to begin the reconditioning of one of the dilution fridges in the "Low temperature laboratory" in the Faculty of Science.

The dilution fridge was successfully equipped with a Ruthenium(IV) oxide (RuO_2) thermometer to monitor the temperature of the sample (see Figure 28). The thermometer was mounted on the insert of the dilution fridge, close to where the sample is mounted (far-right part in Figure 28).

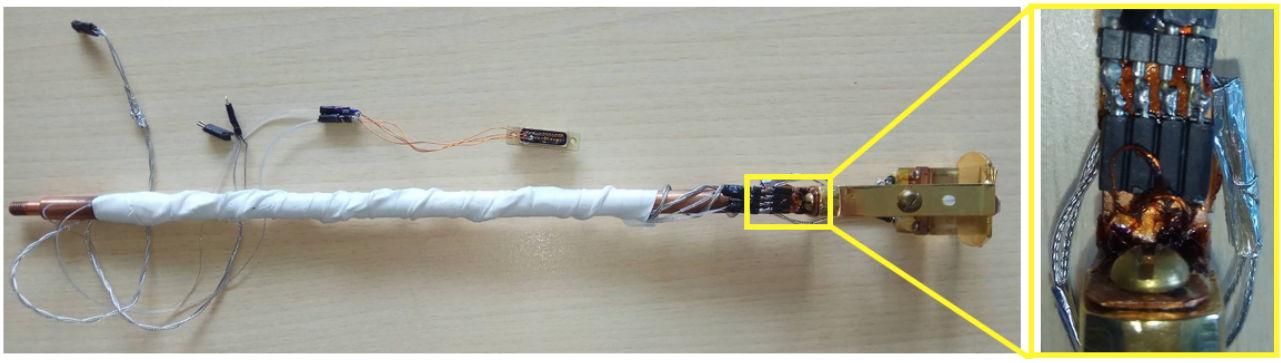

Figure 28. Left: insert of the dilution fridge. The far-right end part of the insert is the sample holder, where the sample is placed for the magnetic measurements. Right: close-up view of the thermometer.

Bibliography

[1] M.A. Sessoli, R. Gatteschi, D. Caneschi, A. Novak, Nature 365 (1993) 141–143.

[2] T. Lis, Acta Crys (1980) 2042–2046.

[3] J.D. Rinehart, J.R. Long, Chem. Sci. (2011) 2078–2085.

[4] J. Liu, Y. Chen, J. Liu, V. Vieru, L. Ungur, J. Jia, M. Tong, JACS (2016).

[5] S.K. Gupta, G.R. Thayalan Rajeshkumar, Chem. Sci. (2016) 1–11.

[6] R.J. Blagg, L. Ungur, F. Tuna, J. Speak, P. Comar, D. Collison, W. Wernsdorfer, E.J.L. Mcinnes, L.F. Chibotaru, R.E.P. Winpenny, Nat. Chem. (2013) 1–6.

[7] W. Huang, F. Shen, S. Wu, L. Liu, D. Wu, Z. Zheng, J. Xu, M. Zhang, X. Huang, J. Jiang, F. Pan, Y. Li, K. Zhu, O. Sato, Inorg. Chem. (2016).

[8] M. Mannini, F. Pineider, P. Sainctavit, C. Danieli, E. Otero, C. Sciancalepore, A.M. Talarico, M. Arrio, A. Cornia, D. Gatteschi, R. Sessoli, Nat. Mater. 8 (2009) 194–197.

[9] L. Wernsdorfer, W. Bogani, Nature 7 (2008) 179–186.

[10] A. Candini, S. Klyatskaya, M. Ruben, W. Wernsdorfer, A. Marco, (2011) 2634–2639.

[11] M.N. Leuenberger, D. Loss, Lett. to Nat. 410 (2001) 789–793.

[12] J.W. Rohlf, Modern Physics from a to Z0, Wiley, 1994.

[13] H.A. Kramers, Proc. Acad. Sci. Amsterdam 33, p. 959 (1930).

[14] S. Blundell, Magnetism in Condensed Matter, Oxford University Press, 2001.

[15] G. Christou, D. Gatteschi, D.N. Hendrickson, R. Sessoli, MRS Publ. (2000) 66–71.

[16] V.I. Waller, Phys. Inst. Der Eifg. Techn. (1932) 370–388.

[17] A.H. Morrish, The Physical Principles of Magnetism, IEEE Press, University of Manitoba, Canada, 2001.

[18] J.. Bartolomé, J. Fernando Luis, Fernández, Molecular Magnets, Physics and Applications, Springer, 2014.

[19] J.R. Friedman, M.P. Sarachik, Phys. Rev. Lett. 1 (1996) 1–4.

[20] E. Bartolomé, A. Araúzo, J. Luzón, J. Bartolomé, F. Bartolomé, Handb. Magn. Mater. 26 (2017).

[21] H.A. Kramers, R. Kronig, in:, Atti Del Congr. Int. Fis. Como, 1927.

[22] K.S. Cole, R.H. Cole, J. Chem. Phys. 341 (1941) 341–351.

[23] Y.-N. Guo, G.-F. Xu, Dalt. Trans. 40 (2011) 9953–9963.

[24] O. Kahn, Molecular Magnetism, VCH Publishers, 1993.

[25] R.L. Carlin, Magnetochemistry, Springer-Verlag Berlin Heidelberg, 1986.

[26] J.J. Borrás-Almenar, J.M. Clemente-Juan, E. Coronado, B.S. Tsukerblat, J. Comput. Chem. 22 (2000) 985–991.

[27] S. Jank, H. Reddmann, H. Amberger, Inorganica Chim. Acta 361 (2008) 2154–2158.

[28] N.F. Chilton, D. Collison, E.J.L. McInnes, R.E.P. Winpenny, A. Soncini, Nat. Commun. 4 (2013) SI.

[29] N.F. Chilton, D. Collison, E.J.L. Mcinnes, R.E.P. Winpenny, A. Soncini, Nat. Commun. 4 (2013) 1–7.

[30] J.A. Giordmaine, F.R. Nash, Phys. Rev. 138 (1965) 1510–1523.

[31] P.L. Scott, C.D. Jeffries, Phys. Rev. 127 (1962) 32–50.

[32] A. Watanabe, A. Yamashita, M. Nakano, T. Yamamura, Chem. a Eur. J. 189 (2011) 7428–7432.

[33] C. Aronica, G. Pilet, G. Chastanet, W. Wernsdorfer, J. Jacquot, D. Luneau, Angew. Chemie (2006) 4659–4662.

[34] M.D. Jenkins, D. Zueco, O. Roubeau, G. Aromí, J. Majer, F. Luis, Dalt. Trans. 45 (2016) 16682–16693.

[35] Q. Design, (1999) 62.

[36] M. Higuchi, J. Magn. Magn. Mater. 181 (1998) 439–440.